JACS
JOURNAL OF THE AMERICAN CHEMICAL SOCIETY
Article
pubs.acs.org/JACS

Valence Band Modification and High Thermoelectric Performance in SnTe Heavily Alloyed with MnTe

Gangjian Tan,[†] Fengyuan Shi,[‡] Shiqiang Hao,[‡] Hang Chi,[§] Trevor P. Bailey,[§] Li-Dong Zhao,[∥] Ctirad Uher,[§] Chris Wolverton,[‡] Vinayak P. Dravid,[‡] and Mercouri G. Kanatzidis*[,†,⊥]

[†]Department of Chemistry, Northwestern University, Evanston, Illinois 60208, United States
[‡]Department of Materials Science and Engineering, Northwestern University, Evanston, Illinois 60208, United States
[§]Department of Physics, University of Michigan, Ann Arbor, Michigan 48109, United States
[∥]School of Materials Science and Engineering, Beihang University, Beijing 100191, China
[⊥]Materials Science Division, Argonne National Laboratory, Argonne, Illinois 60439, United States

Supporting Information

ABSTRACT: We demonstrate a high solubility limit of >9 mol% for MnTe alloying in SnTe. The electrical conductivity of SnTe decreases gradually while the Seebeck coefficient increases remarkably with increasing MnTe content, leading to enhanced power factors. The room-temperature Seebeck coefficients of Mn-doped SnTe are significantly higher than those predicted by theoretical Pisarenko plots for pure SnTe, indicating a modified band structure. The high-temperature Hall data of $Sn_{1-x}Mn_xTe$ show strong temperature dependence, suggestive of a two-valence-band conduction behavior. Moreover, the peak temperature of the Hall plot of $Sn_{1-x}Mn_xTe$ shifts toward lower temperature as MnTe content is increased, which is clear evidence of decreased energy separation (band convergence) between the two valence bands. The first-principles electronic structure calculations based on density functional theory also support this point. The higher doping fraction (>9%) of Mn in comparison with ∼3% for Cd and Hg in SnTe gives rise to a much better valence band convergence that is responsible for the observed highest Seebeck coefficient of ∼230 μV/K at 900 K. The high doping fraction of Mn in SnTe also creates stronger point defect scattering, which when combined with ubiquitous endotaxial MnTe nanostructures when the solubility of Mn is exceeded scatters a wide spectrum of phonons for a low lattice thermal conductivity of 0.9 W m^{-1} K^{-1} at 800 K. The synergistic role that Mn plays in regulating the electron and phonon transport of SnTe yields a high thermoelectric figure of merit of 1.3 at 900 K.

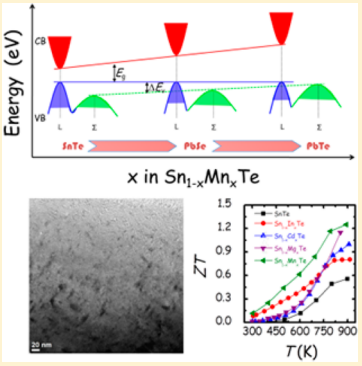

INTRODUCTION

Lead chalcogenides and their solid solutions are among the most efficient thermoelectric materials in the mid- to high-temperature region, with the maximum figure of merit ZT exceeding 2.[1−5] Despite their excellent environmental stability, the perceived toxicity of lead chalcogenides can frustrate their development and large-scale application. In this context, SnTe, which resembles PbTe in many respects [rock-salt crystal structure above room temperature,[6] two-valence-band character,[7−9] fairly good mechanical properties (Young's modulus, 55.6 GPa for SnTe vs 58.1 GPa for PbTe; shear modulus, 21.7 GPa for SnTe vs 23.0 GPa for PbTe; hardness, 0.78 GPa for SnTe vs 0.76 GPa for PbTe),[10] etc.] is attracting increasing attention as a possible substitute of PbTe for thermoelectric power generation.[11−22] Moreover, experimentally, the high-temperature (300−663 K) Young's modulus and shear modulus measurements on SnTe show no significant hysteresis between the heating and cooling curves, indicating the absence of any microcracking or bloating.[10] This is of great importance, with implications on device stability.

SnTe has been historically viewed as an inferior p-type thermoelectric leg[7,8,23−27] in comparison to PbTe because of its lower Seebeck coefficient. The latter is due to (i) heavy intrinsic doping arising from spontaneous Sn vacancies in the structure and (ii) a large energy separation ΔE_v between the higher lying light hole band at the L point and the lower-lying heavy hole band at the Σ point which limits hole transport to a single band, giving a low Seebeck coefficient. For example, this ΔE_v is ∼0.35 eV for SnTe[7,8,23] vs ∼0.17 eV for PbTe[9,28] at 300 K. SnTe also has a higher lattice thermal conductivity (∼3.5 W m^{-1} K^{-1} for SnTe vs 1.5 W m^{-1} K^{-1} for PbTe[29] at 300 K) because Sn is lighter than Pb. However, recent studies unambiguously show that SnTe has a strong potential of being a promising thermoelectric through band engineering and/or all-scale hierarchical architecturing[11−15,19] (see Table 1). Specifically, it has been shown that In doping modifies the band structure of SnTe by creating resonant levels in the valence bands, thus considerably increasing the Seebeck coefficient, especially in the low- to mid-temperature range.[11,13] Cd, Hg, and Mg dopants, on the other hand, can enhance the Seebeck coefficient of p-type SnTe through convergence of the two valence bands

Received: July 13, 2015

DOI: 10.1021/jacs.5b07284
J. Am. Chem. Soc. XXXX, XXX, XXX−XXX

Table 1. Recent Progress in SnTe-Based Thermoelectric Materials

ref	dopant	toxicity	solubility (%)	band structure modification	hierarchical architectures microstructuring	highest ZT
12	Cd	yes	~3	band convergence	point defect + CdS nanostructuring	1.3@873 K
14	Hg	yes	~3	band convergence	point defect	1.3@923 K
13	In and Cd	yes	~3	synergy of resonant levels and band convergence	point defect + CdS nanostructuring	1.4@923 K
11	In	**no**	<1	resonant levels	point defect + grain size refinement	1.1@873 K
15	Ag and Bi	**no**	n/a	n/a	point defect + nanostructuring	1.1@800 K
this study	Mn	**no**	>9	band convergence	point defect + MnTe nanostructuring	**1.3@900 K**

which is of particular significance at high temperatures.[12−14,19] These two effects can coexist in p-type SnTe via In and Cd co-doping, contributing to a wide temperature enhancement of the Seebeck coefficient.[13] Microstructuring processes, including alloying,[14,15,19] grain size refinement,[11] and second phase nanostructuring,[12,13,15] offer other avenues to improve SnTe performance by scattering heat-carrying phonons. The synergy of these approaches yields a record high ZT of ~1.4 at 923 K in p-type In and Cd co-doped SnTe nanostructured with CdS.[13]

Mn has been well explored in p-type PbTe for its role in effectively diminishing the energy offsets between the two valence bands.[30−32] There are several reports on Mn-doped SnTe regarding its interesting magnetic properties;[33−36] however, to the best of our knowledge, studies on their thermoelectric properties are scarce.[37] The similarities in crystal and band structures between SnTe and PbTe suggest the possibility that Mn causes the light and heavy hole bands of SnTe to converge as in PbTe.

In this study, for the first time, we systematically and comprehensively investigate the band structures and high-temperature thermoelectric properties of SnTe where the Sn sites in the lattice are alloyed with Mn, using both experimental and computational tools. We show that, like with Cd and Hg,[12−14] the introduction of Mn in the structure significantly alters the bands of SnTe by decreasing ΔE_v and enlarging the band gap E_g. However, the much higher solubility of >9 mol% for Mn (compared to only ~3 mol% for Cd and Hg dopants[12,14]) in SnTe gives a much better valence band convergence. Doping-induced band convergence is dependent on the amount of dopant[38,39] and is responsible for the high Seebeck coefficients (for example, ~78 and ~230 μV/K at 300 and 900 K, respectively, observed for 12 mol% Mn-doped SnTe). These are in fact comparable to those of p-type PbTe[40] with a similar hole concentration. We also show that alloy scattering by Mn/Sn substitution together with the interfacial scattering by MnTe-rich nanoprecipitates (when Mn exceeds its solubility limit) largely suppresses the phonon propagation in SnTe, synergistically leading to a strongly reduced lattice thermal conductivity. This yields a high figure of merit ZT of ~1.3 at 900 K in the sample with a nominal composition of $Sn_{0.88}Mn_{0.12}Te$, outperforming any other singly doped SnTe.

EXPERIMENTAL SECTION

Synthesis. High-purity Sn chunk (99.9999%, American Elements, USA), Mn pieces (99.9%, Alfa Aesar, USA), and Te shot (99.999%, 5N Plus, Canada) were used as the starting materials to synthesize 8 g of $Sn_{1-x}Mn_xTe$ (x = 0, 0.01, 0.02, 0.03, 0.05, 0.07, 0.09, 0.11, 0.12, 0.13, 0.14, and 0.15 in mole ratio). Desired amounts of Sn, Mn, and Te were weighed and flame-sealed in 13 mm diameter fused silica tubes under a residual pressure of ~10^{-4} Torr. The loaded tubes were then melted in a computer-controlled furnace with a heating profile as described below: the samples were heated to 1423 K in 11 h, soaked at this temperature for 12 h, and then quickly cooled down to room temperature by quenching the sample in ice water. The tubes containing the molten samples were periodically shaken to ensure the homogeneity of the compositions. The quenched ingots were annealed at 873 K for another 2 days and then ground into fine powders using a mechanical grinder. The powders were then put inside a 12.7 mm diameter graphite die and densified by spark plasma sintering (SPS, SPS-211LX, Fuji Electronic Industrial Co., Ltd.) at 773 K for 5 min under an axial compressive stress of 40 MPa in a vacuum. Highly dense disk-shaped pellets with dimensions of 12.7 mm diameter and ~9 mm thickness were obtained.

Electron Microscopy and X-ray Diffraction. (Scanning) transmission electron microscopy ((S/TEM) and STEM energy-dispersive spectroscopy (EDS) experiments were carried out using a JEOL 2100F microscope operated at 200 kV. The thin TEM specimens were prepared by conventional methods, including cutting, grinding, dimpling, and tripod, with minimal duration of Ar-ion milling with a liquid N_2 cooling stage. Samples pulverized with an agate mortar were used for powder X-ray diffraction (PXRD). The powder diffraction patterns were obtained with Cu Kα (λ = 1.5418 Å) radiation in a reflection geometry on an Inel diffractometer operating at 40 kV and 20 mA and equipped with a position-sensitive detector.

Physical Characterization. *Electrical Properties.* The obtained SPS-processed pellets were cut into bars with dimensions 12 × 3 × 3 mm^3 for simultaneous measurement of the Seebeck coefficient and electrical conductivity using an Ulvac Riko ZEM-3 instrument under a low-pressure helium atmosphere from room temperature to 900 K. Samples were spray-coated with boron nitride spray to minimize outgassing, except where needed for electrical contact with the thermocouples, heater, and voltage probes. The uncertainty of the Seebeck coefficient and electrical conductivity measurements is 5%.[41]

Thermal Conductivity. Highly dense SPS-processed pellets were cut and polished into a square shape of 6 × 6 × 2 mm^3 for thermal diffusivity measurements. The samples were coated with a thin layer of graphite to minimize errors from the emissivity of the material. The total thermal conductivity was calculated from $\kappa_{tot} = DC_pd$, where the thermal diffusivity coefficient (D) was measured using the laser flash diffusivity method in a Netzsch LFA457 instrument, and the density (d) was determined using the dimensions and mass of the sample. The specific heat capacity (C_p) of SnTe[13] was adopted for all the samples in this study. The thermal diffusivity data were analyzed using a Cowan model with pulse correction. The measured densities of all the samples range between 6.1 and 6.3 g cm^{-3} or are above 96% of the theoretical densities (see Table S1). The uncertainty of the thermal conductivity is estimated to be within 8%, considering all the uncertainties from D, C_p, and d.[41] The thermal diffusion data for all samples can be found in Figure S1. The lattice thermal conductivity (κ_{lat}) was calculated by subtracting the electrical thermal conductivity (κ_{ele}) from κ_{tot} using the Wiedemann−Franz relationship, $\kappa_{ele} = L\sigma T$, where L is the Lorenz number (Figure S2) which can be obtained by fitting the Seebeck coefficient to the reduced chemical potential.[42−45] The combined uncertainty for all measurements involved in the calculation of ZT is less than 15%. Unless otherwise noted, all the thermoelectric properties were measured perpendicular to the sintering pressure direction, although no directional anisotropy effects (less than 3%) were observed in the charge transport properties.

Hall Measurements. The high-temperature Hall measurement was performed on a home-made apparatus (University of Michigan) in an argon atmosphere. The Hall resistance was monitored with a Linear

DOI: 10.1021/jacs.5b07284
J. Am. Chem. Soc. XXXX, XXX, XXX−XXX

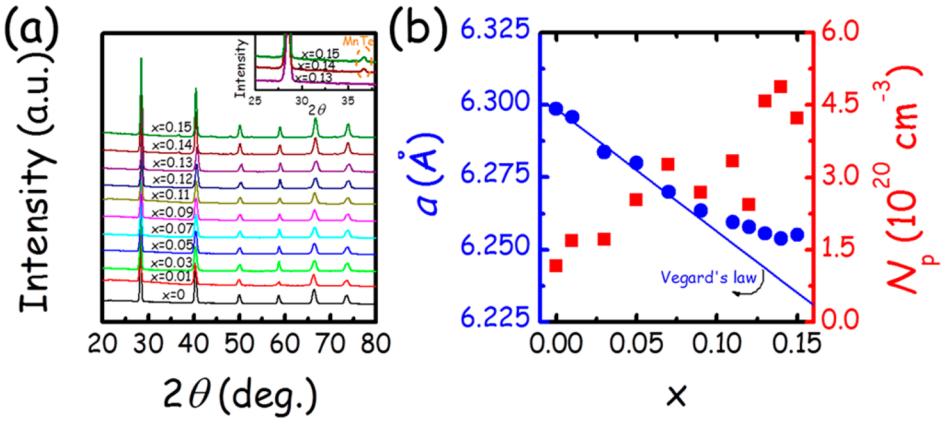

Figure 1. (a) Powder XRD patterns for samples of $Sn_{1-x}Mn_xTe$ in this study; inset is a zoom-in view of the PXRD (2θ ranging between 25° and 38°) for samples with x = 0.13−0.15 clearly showing the presence of MnTe second phase around 2θ = 36.5° starting with the x = 0.14 sample. (b) Room-temperature lattice parameter (a, left y axis, in blue symbols and fonts) and hole concentration (N_p, right y axis, in red symbols and fonts) as a function of Mn alloying fraction x.

Research AC resistance bridge (LR-700), with constant magnetic fields of ±1 T applied by using an Oxford superconducting magnet. The effective carrier concentration (N_p) was estimated using the relationship $N_p = 1/eR_H$, where e is the elemental charge and R_H is the Hall coefficient. The Hall mobility (μ_H) was calculated using the relationship $\mu_H = \sigma R_H$, with σ being the electrical conductivity obtained from the ZEM-3 instrument.

Band Structure Calculations. Density functional theory (DFT) calculations of pristine SnTe and Mn-doped SnTe were carried out. The calculations were performed using the generalized gradient approximation with PBE[46] functional for the exchange-correlation functional and projector-augmented wave potentials as implemented in Vienna Ab initio Simulation Package (VASP).[47] All structures are fully relaxed with respect to cell vectors and cell-internal positions. The total energies were numerically converged to approximately 3 meV/cation using a basis set energy cutoff of 400 eV and dense k-meshes corresponding to 4000 k-points per reciprocal atom in the Brillouin zone. To investigate the movements of the conduction band and valence bands (L and Σ bands), we considered 3×3×3 supercells of NaCl type $Sn_{27}Te_{27}$. Even though Mn has been explored as multivalent species (+2, +3, +4, etc.), we consider Mn in SnTe as an isovalent doping with Mn substituting for Sn.[48,49] The scalar relativistic spin polarization effect has been considered with an initial magnetic moment of 5 μ_B for the substituted Mn. The substitution defects in SnTe completely change the symmetry of the original primitive cell. Thus, for the purposes of a more direct comparison with SnTe we transformed the eigenstates for defect structures into a so-called effective band structure in the primitive Brillouin zone of the parent compound SnTe using a spectral decomposition method.[50,51] Using this approach, we are able to calculate the energy level of the L-point and Σ-line and the corresponding energy differences for the supercells with defects.

RESULTS AND DISCUSSION

Doping/Alloying Chemistry of Mn in SnTe. Figure 1a shows the PXRD patterns of $Sn_{1-x}Mn_xTe$. Single phase compounds with a rock-salt SnTe structure are confirmed within the instrument detection limit when $x \leq 0.13$, and beyond that, a MnTe second phase clearly shows up, see inset. The lattice parameter (a, left y axis) shown in Figure 1b decreases with increasing Mn content, consistent with the smaller radius of Mn^{2+} (0.66 Å, Mn is regarded as Mn^{2+} in SnTe and PbTe[48,49]) compared to that of Sn^{2+} (0.93 Å). Vegard's law, denoted by the solid line, describes well the variation of lattice parameter for $Sn_{1-x}Mn_xTe$ up to x = 0.09, exceeding which a clear deviation from such a linear trend is observed. This suggests a complete solid solution between SnTe and MnTe for $x \leq 0.09$. For $x > 0.09$, SnTe-MnTe is partly alloyed and partly phase separated. Note here that the solubility limit of Mn (at least 9 mol%) in SnTe is an estimate only using the XRD data. As we have pointed out in previous publications, the limit might be lower and to probe this one generally needs high-resolution TEM to check for nanostructures.[4,15,52−54] This PXRD estimated solubility limit of Mn in SnTe is substantially larger than that of Cd and Hg (~3 mol %)[12,14] and is by and large consistent with an earlier report by Dudkin.[55]

The room-temperature Hall concentrations (N_p, right y axis) as a function of x for $Sn_{1-x}Mn_xTe$ are displayed in Figure 1b. N_p increases with increasing x until 0.07, becomes relatively constant when x is between 0.09 and 0.12, and increases again afterward. The variation of N_p reasonably supports the ~9 mol % solubility of Mn in SnTe. One can also conclude that Mn serves as an electron acceptor in SnTe within the doping limit, although its use was meant to be isovalent with Sn.[48,49] A similar phenomenon was observed with Cd,[12] Hg,[14] and Mg[19] dopants in SnTe. This doping behavior is unusual and may arise from a modulating effect of the M^{2+} dopant ion on the degree of Sn vacancy formation.[56,57]

Thermoelectric Properties of $Sn_{1-x}Mn_xTe$. The temperature-dependent electrical conductivity and Seebeck coefficient for $Sn_{1-x}Mn_xTe$ samples are shown in Figure 2a,b. The electrical conductivity decreases while the Seebeck coefficient increases with increasing temperature for all the samples, consistent with degenerately doped semiconductors.

Figure 2c shows the room-temperature Hall mobility (μ_H) as a function of temperature for $Sn_{1-x}Mn_xTe$. It is clearly seen that μ_H decreases systematically upon Mn alloying which accounts for the reduced electrical conductivity (Figure 2a) as the Mn content increases. The gradual loss of mobility in SnTe with increasing Mn content is caused by a number of factors including (i) increased point defect scattering within solid solution, (ii) magnetic scattering, (iii) interfacial scattering caused by Mn-rich nanoprecipitates (see below) for $x > 0.09$, and (iv) enhanced density of states effective mass of holes caused by Mn-induced valence band convergence. The latter will be discussed in the next section.

It is counterintuitive when the Seebeck coefficient of SnTe increases with increasing Mn content (Figure 2b) because the

DOI: 10.1021/jacs.5b07284
J. Am. Chem. Soc. XXXX, XXX, XXX−XXX

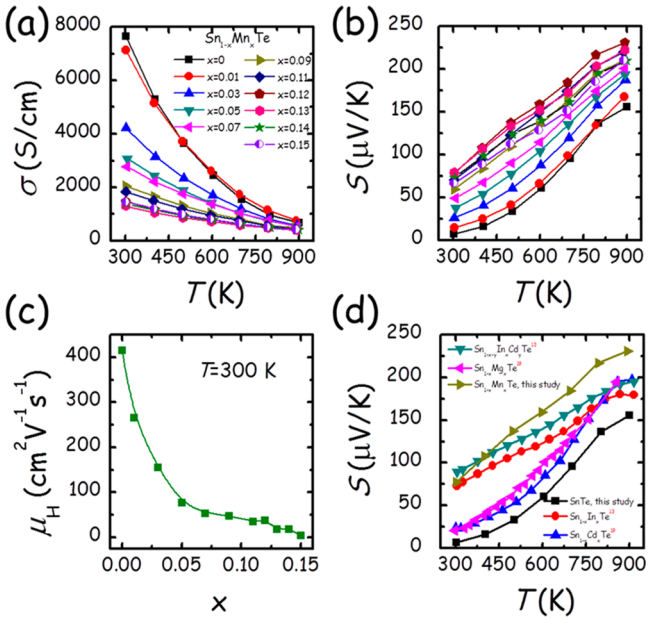

Figure 2. Temperature-dependent (a) electrical conductivity and (b) Seebeck coefficient for $Sn_{1-x}Mn_xTe$. (c) Room-temperature carrier mobility (μ_H) as a function of Mn alloying fraction x. (d) Comparison of the temperature-dependent Seebeck coefficients of SnTe with different dopants,[13,19] among which Mn-doped SnTe clearly shows the highest value.

hole density also increases in this process (Figure 1b), if we assume a single parabolic band model.[58] This abnormal trend could be partly interpreted by the specific behavior of the two-valence-band character of SnTe.[7,8,23] When more holes are activated, the Fermi level is pushed deeper into the valence band of SnTe so that the second heavy hole band begins to contribute in an increasing manner. This gives rise to a positive dependence of hole concentration (in the range of $(1-5) \times 10^{20}$ cm^{-3}) on the Seebeck coefficient, as shown in the theoretical Pisarenko plot[11] in Figure 6a, below.

Figure 2d compares the temperature-dependent Seebeck coefficients of several singly doped SnTe compositions.[13,19] The alloying of either In[13] or Cd/Mg[13,19] in Sn lattice sites can significantly enhance the Seebeck coefficient of SnTe because of the resonant levels introduced inside the valence bands and the resultant valence band convergence of SnTe. Combining In and Cd dopants in SnTe results in an even higher Seebeck coefficient over a broad temperature range due to the synergy of these two effects.[13] Surprisingly, we found that Mn-doped SnTe has the highest Seebeck coefficient yet among them almost over the full temperature range (300−900 K). For example, the Seebeck coefficient of $Sn_{1-x}Mn_xTe$ is ~78 μV/K at room temperature, which is comparable to that of In singly doped (~75 μV/K) and that of In/Cd co-doped SnTe (~86 μV/K). With increasing temperature it increases almost linearly and reaches ~230 μV/K at 900 K. In comparison pure SnTe has ~150 μV/K, $Sn_{1-x}In_xTe$ has ~180 μV/K, and $Sn_{1-x}Cd_xTe$ or $Sn_{1-x-y}In_xCd_yTe$ have ~200 μV/K at 900 K.[13] This record high Seebeck coefficient achieved in Mn-doped SnTe is attributed to the stronger valence band convergence caused by the high fraction of Mn dopants, as we will elaborate below.

The temperature-dependent power factors of $Sn_{1-x}Mn_xTe$ are plotted in Figure 3. They increase steadily with increasing Mn content up to x = 0.12 because of the largely improved Seebeck coefficient. Note here that the power factors achieved

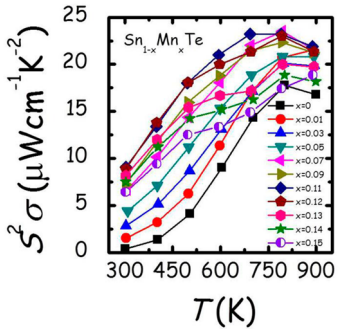

Figure 3. Temperature-dependent power factors for $Sn_{1-x}Mn_xTe$.

with Mn-doped SnTe are comparable to or even better than those of PbTe.[2,3,40] At x > 0.12 the power factors saturate gradually due to the presence of excessive MnTe second phase (Figure 1a) which deteriorates the carrier mobility (Figure 2c) and through it the electrical conductivity (Figure 2a) while the Seebeck coefficient is only little altered in this process (Figure 2b).

The total and lattice thermal conductivities for $Sn_{1-x}Mn_xTe$ are shown in Figures 4a,b as a function of temperature, respectively. Both quantities show negative change as Mn content rises. The x = 0 and 0.01 samples show clear bipolar conduction around 500 K which however becomes negligible for $x \geq 0.03$. The reasons for this are 2-fold: (1) the increase of hole concentration with increasing Mn content (Figure 1b) suppresses the population of minority carriers; (2) the band bap enlargement by Mn alloying inhibits the thermal excitation of holes across the forbidden gap at high temperature. While it is challenging to experimentally determine the optical band gaps of $Sn_{1-x}Mn_xTe$ because of the strong interference from the large population of free carriers, we here compare the temperature-dependent lattice thermal conductivities of SnTe[13] and $Sn_{0.97}Mn_{0.03}Te$ with a similar N_p of ~1.8×10^{20} cm^{-3} at 300 K, Figure 4c, in order to probe the role of the band gap. Clearly, the bipolar conduction of SnTe is largely suppressed by Mn alloying, indicative of a larger band gap being at play. In the next section, the first-principles band structure calculation results support this point. It should be noted that the strong reduction of lattice thermal conductivity of SnTe upon Mn alloying is absent in Cd-[12,13] or In-doped [11,13] SnTe where there is only a moderate effect. The much higher doping fraction of Mn and the more significant atomic mass difference between Mn and Sn are likely responsible for this, according to eq 2 shown below.

The magnitude of room-temperature lattice thermal conductivity for $Sn_{1-x}Mn_xTe$ has a clear declining trend as the Mn content increases, Figure 4d. Based on Klemens's model,[59] the lattice thermal conductivity of a disordered alloy can be expressed by

$$\frac{\kappa_{lat,disorder}}{\kappa_{lat,pure}} = \frac{\arctan u}{u}, \quad \text{and} \quad u^2 = \frac{\pi^2 \Theta_D \Omega}{h\nu^2} \kappa_{lat,pure} \Gamma \tag{1}$$

where $\kappa_{lat,disorder}$ and $\kappa_{lat,pure}$ represent the lattice thermal conductivities of disordered alloys (Mn-doped SnTe in this study) and pure alloy (undoped SnTe in this study) respectively, u is the disorder scaling parameter, Θ_D is the Debye temperature (~140 K for SnTe[60]), Ω is the volume per atom, h is the Planck constant, ν is the average sound velocity

DOI: 10.1021/jacs.5b07284
J. Am. Chem. Soc. XXXX, XXX, XXX−XXX

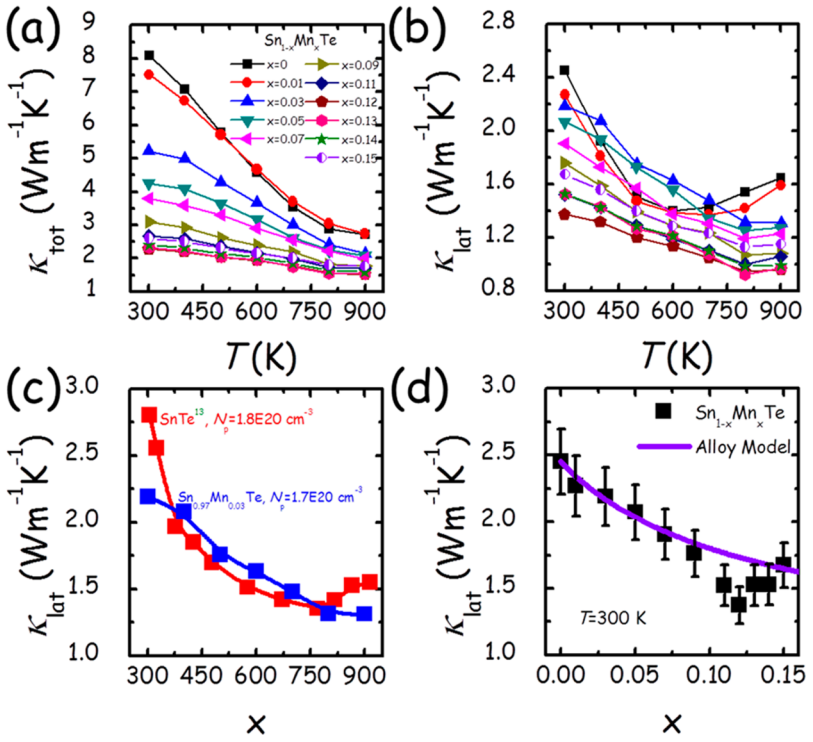

Figure 4. Temperature-dependent (a) total and (b) lattice thermal conductivities for $Sn_{1-x}Mn_xTe$. (c) A comparison of temperature dependence of lattice thermal conductivity for SnTe[13] and $Sn_{0.97}Mn_{0.03}Te$ with a similar carrier concentration at room temperature demonstrating the positive role of band gap enlargement of SnTe enabled by Mn alloying in suppressing the bipolar conduction. (d) Room-temperature lattice thermal conductivity as a function of Mn alloying fraction x for $Sn_{1-x}Mn_xTe$, 10% error bars are indicated. The solid line is the modeled lattice thermal conductivities of $Sn_{1-x}Mn_xTe$ based on an alloy model.[62,63]

(~1800 m/s for SnTe[61]), and Γ is the scattering parameter that combines the influences from mass, bonding force, and strain contrasts, described as

$$\Gamma = x(1-x)\left[\left(\frac{\Delta M}{M}\right)^2 + \varepsilon\left(\frac{a_{\text{disorder}} - a_{\text{pure}}}{x a_{\text{pure}}}\right)^2\right] \quad (2)$$

here x is the doping fraction, $\Delta M/M$ is the rate of change of atomic mass, a_{disorder} and a_{pure} denote the lattice constants of disordered and pure alloys respectively, and ε is an elastic properties related adjusting parameter that can be estimated by[62,63]

$$\varepsilon = \frac{2}{9}\left[(G + 6.4\gamma)\frac{1+r}{1-r}\right]^2 \quad (3)$$

where G is a ratio between the relative change of bulk modulus and the bonding length and can be usually taken as a constant value of 3 for IV–VI semiconductors,[64,65] γ is the Grüneisen parameter (2.1 for SnTe[66]), and r is the Poisson ratio (0.244 for SnTe[10]). These yield an ε value of ~163 for SnTe on the basis of eq 3, which when combined with eqs 1 and 2, can model the composition-dependent lattice thermal conductivities of $Sn_{1-x}Mn_xTe$ as the solid line shown in Figure 4d. It can be seen that most of the experimental points agree well with the modeling, supporting the idea that the point defect scattering caused by Mn alloying is a dominant factor contributing to the decreased lattice thermal conductivity seen in $Sn_{1-x}Mn_xTe$. However, a clear departure from the model can be observed for the samples with $x > 0.09$. We will show later that the presence of the coherent Mn-rich nanoprecipitates (acting as effective phonon scattering medium) when Mn exceeds its solubility limit contributes to additional reduction of lattice thermal conductivity in these samples.

Benefiting from the enhanced power factor and decreased thermal conductivity, the ZT value of SnTe is systematically increased upon Mn alloying, Figure 5a. A maximum ZT of ~1.3 at 900 K is achieved in the $Sn_{0.88}Mn_{0.12}Te$ sample, which is much superior to any other singly doped SnTe[13,19] (Figure 5b) and also outperforms other p-type lead-free thermoelectric materials[67−71] (Figure 5c). Figure 5d compares the 300−900 K average ZT values (ZT_{ave}) of several singly doped SnTe materials, among which $Sn_{1-x}Mn_xTe$ clearly outperforms any others. More importantly, this high-performing composition appears very stable in the heating−cooling thermal cycles, which is important for actual application, Figure S3.

Band Tuning of SnTe by MnTe Alloying. Figure 6a shows the room-temperature Seebeck coefficient as a function of hole concentration for $Sn_{1-x}Mn_xTe$ and the solid line is a theoretical Pisarenko plot[11] for SnTe calculated on the basis of a two-valence-band model. The data points for undoped[23,24] and Bi-doped[27,72] SnTe can be well described by this theoretical line, suggesting the validity of the model. However, those Mn-containing samples have much higher Seebeck coefficient than predicted by the Pisarenko curve, indicative of a modified band structure. This band modification is Mn-induced valence band convergence, similar to the case in Mn-doped PbTe.[30,31]

In rocksalt IV–VI semiconductors which are known for their two-valence-band character, as temperature rises, the upper light hole band lowers its energy while the lower heavy hole shows negligible energy change, resulting in carriers redistribution between the two bands and a strong temperature

DOI: 10.1021/jacs.5b07284
J. Am. Chem. Soc. XXXX, XXX, XXX−XXX

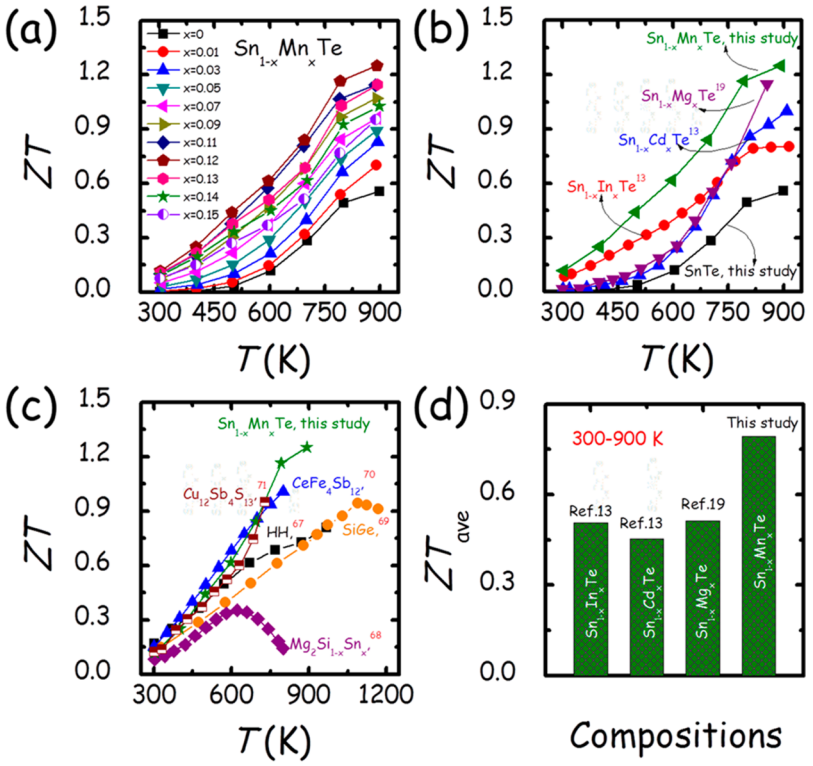

Figure 5. (a) Temperature-dependent ZT values for $Sn_{1-x}Mn_xTe$. (b) Comparison of the ZT values of several singly doped SnTe,[13,19] among which Mn-doped SnTe clearly has the highest performance in the entire temperature range because of the stronger valence band convergence by higher doping limit of Mn. (c) Comparison of temperature-variant ZT of Mn-doped SnTe with some other p-type lead-free systems including half-Heusler compound (HH),[67] $Mg_2Si_{1-x}Sn_x$,[68] SiGe alloy,[69] skutterudite ($CeFe_4Sb_{12}$),[70] and a presentative of tetrahedrites ($Cu_{12}Sb_4S_{13}$).[71] (d) Comparison of average ZT (ZT_{ave}) in the temperature interval of 300−900 K of several singly doped p-type SnTe,[13,19] among which Mn-doped SnTe has a ZT_{ave} that outperforms any others.

dependence of the Hall coefficient R_H.[73−75] R_H peaks when the contribution from two types of carriers with different effective masses to conduction is equal.[76] Therefore, the peak temperature (T_{peak}, which is usually independent of carrier concentrations[77]) of R_H is an important measure of the energy separation between bands (but is not equivalent to the band convergence temperature (T_{cvg}) which should be even higher than T_{peak}). Figure 6b presents the temperature-dependent Hall coefficients (normalized relative to the room-temperature values) for SnTe, PbSe[78] and PbTe.[3] The peak temperature in the R_H-T curves goes down from ∼750 K for SnTe to ∼700 K for PbSe and then to ∼425 K for PbTe. This sequence of T_{peak} is in accordance with their magnitude of ΔE_v (0.35 eV,[7,8,23] 0.25 eV,[78] and 0.17 eV,[9,28] respectively, for the three at 300 K). In contrast, p-type PbS[79] which is usually taken as a conventional one-valence-band semiconductor shows a nearly temperature-independent R_H, Figure 6b.

The temperature-dependent normalized R_H for the $Sn_{1-x}Mn_xTe$ samples are presented in Figure 6c. All samples show a strongly temperature-dependent R_H and T_{peak} shifts steadily toward lower temperature as more Mn is introduced. These data unambiguously demonstrate the two-valence-band structure of SnTe and the ability of Mn alloying to significantly decrease the energy offset between the two valence bands. In our previous study, we showed that alloying with Cd and Hg also converges the light and heavy hole bands of SnTe but the solubility limit of these two elements is much lower (3 mol%) than that of Mn.[12] Therefore, because of its higher concentration in the rocksalt lattice Mn achieves a better band convergence.[38,39]

The temperature dependence of the normalized R_H for 3 mol % Cd-doped SnTe[12] is included in Figure 6c for comparison and shows that R_H peaks at around 650 K in the curve. The T_{peak} of $Sn_{0.97}Cd_{0.03}Te$ is very close to that of $Sn_{0.97}Mn_{0.03}Te$ (∼620 K) and that of PbSe[39] (∼700 K), indicating a similar ΔE_v among them. Correspondingly, for similar hole concentrations one can observe comparable Seebeck coefficients in the three samples,[13,78] see Figure 6d. Likewise, with a higher doping fraction of Mn ($x \geq 0.09$), the T_{peak} of $Sn_{1-x}Mn_xTe$ is further decreased to the level of PbTe (for example, $Sn_{0.88}Mn_{0.12}Te$ has a T_{peak} of ∼400 K, which is very close to that of PbTe, ∼425 K[3]), and therefore the Seebeck coefficient of heavily Mn-doped SnTe behaves like PbTe[40] at similar hole densities, Figure 6d.

The Mn-induced valence band convergence and band gap enlargement of SnTe can be further supported by first-principles electronic structure calculations based on DFT. Figure 7a,b shows the DFT band structures of undoped SnTe and Mn-doped SnTe respectively (considering one Sn atom substitution by Mn in a 3×3×3 SnTe supercell, equivalent to a 3.7 mol% Mn-doped SnTe). Based on the calculations the introduction of Mn effectively brings the valence band at L and the valence band at Σ closer in energy and pushes the conduction minima at the L point to higher energies, resulting in a valence band convergence and a band gap enlargement. Specifically, ΔE_v and E_g are 0.35 and 0.02 eV, respectively, for pure SnTe and become 0.14 and 0.16 eV for $Sn_{26}Mn_1Te_{27}$. The converged valence bands and enlarged band gap by Mn alloying as indicated by our calculations explain the experimentally observed enhanced Seebeck coefficient (Figures 2b and 6a) and

DOI: 10.1021/jacs.5b07284
J. Am. Chem. Soc. XXXX, XXX, XXX−XXX

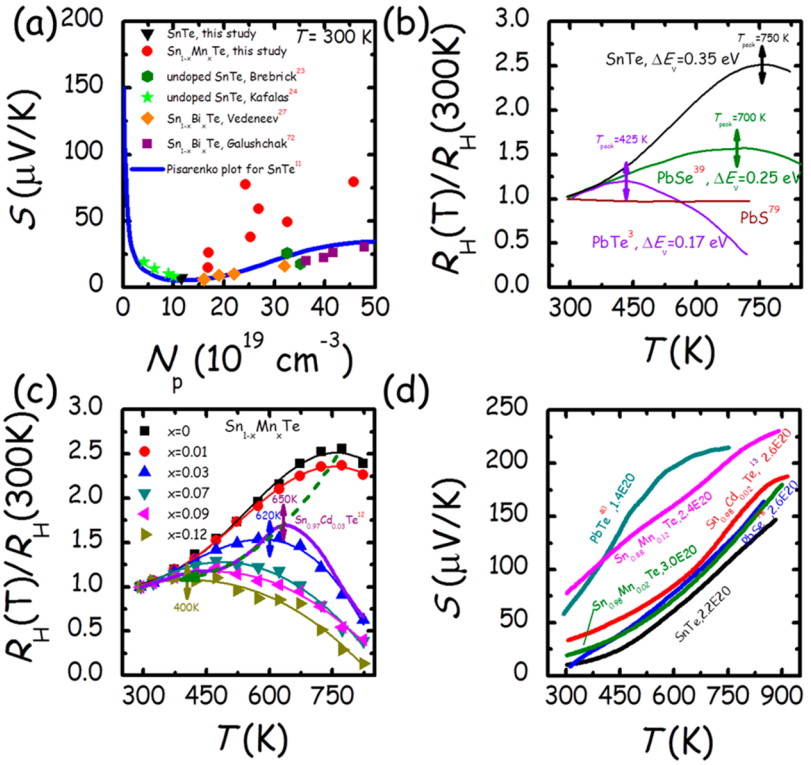

Figure 6. (a) Room-temperature Seebeck coefficients as a function of hole concentration for $Sn_{1-x}Mn_xTe$. The solid line is a theoretical Pisarenko plot of SnTe calculated on the basis of a two-valence-band model.[11] Data for both undoped[23,24] and Bi-doped[27,72] SnTe and from the reported literature agree with this Pisarenko curve but for $Sn_{1-x}Mn_xTe$ it shows a clear deviation (red circles). (b) Hall coefficient (R_H, normalized relative to room-temperature value) for p-type SnTe, PbSe[39] and PbTe[3] show a strong temperature dependence indicative of a two-band conduction. The peaking temperature (T_{peak}) in the R_H-T curves is related to the magnitude of the energy difference (ΔE_v) between the two valence bands. (c) Temperature-dependent Hall coefficients (R_H) for $Sn_{1-x}Mn_xTe$. The lines are guides to the eye. T_{peak} shifts monotonically to lower temperatures as the Mn content rises until $x = 0.12$, indicating a diminished ΔE_v. The temperature dependence of R_H of 3 mol% Cd-doped SnTe[12] is also included for comparison. (d) Comparison of temperature-dependent Seebeck coefficients between p-type doped SnTe[13] and lead chalcogenides[40,78] with similar hole concentrations, demonstrating how the valence band structure of SnTe is transformed to being more PbSe-like and then to PbTe-like as one introduces more amount of band convergence producers (Cd or Mn).

the suppressed bipolar conduction (Figure 4b,c) in $Sn_{1-x}Mn_xTe$. Also note that the calculated ΔE_v value of 0.14 eV for $Sn_{26}Mn_1Te_{27}$ is similar to the 0.12 eV value we previously reported for $Sn_{26}Cd_1Te_{27}$.[12] This suggests that at the same doping level $Sn_{1-x}Mn_xTe$ and $Sn_{1-x}Cd_xTe$ should possess similar physical properties as already presented above. However, because of the much higher solubility of MnTe in SnTe this system can outperform all other doped ones (Figure 5b) reported previously.

With the above data and analysis we are now able to understand how the band structure of SnTe evolves as the Mn alloying fraction increases, Figure 7c. When a moderate amount (e.g., $x < 0.03$) of Mn is doped into SnTe (which can be also realized through Cd or Hg doping), the band gap E_g increases and the energy difference between the two valence bands ΔE_v decreases to the level of PbSe, leading to a performance that is comparable to PbSe (Figure 6d). When a much heavier Mn alloying is realized in SnTe (which however cannot be done in the case of Cd/Hg alloying due to low solubility), the band structure of SnTe can be further tuned to become like PbTe (Figure 6d). This produces the highest Seebeck coefficient reported to date in this system (Figure 2d) and a much higher ZT/ZT_{ave} (Figure 5).

TEM Investigation of $Sn_{0.93}Mn_{0.07}Te$ and $Sn_{0.88}Mn_{0.12}Te$. Microstructures and the compositions of 7% and 12% Mn-doped SnTe samples are investigated by S/TEM and STEM EDS. Figure 8a shows a medium magnification TEM image of $Sn_{0.93}Mn_{0.07}Te$, indicating no obvious nanoscale precipitates in the matrix, consistent with the PXRD results shown in Figure 1a. The inset selected area electron diffraction (SAED) pattern along the [110] orientation shows strong thermal diffuse scattering around diffraction spots, suggesting strong point defect scattering in the sample.[80] The HRTEM image of Figure 8b shows a high-quality sample with minimum damage by the sample preparation procedure. For the 12% Mn doped SnTe sample, on the other hand, nanoscale precipitates were found embedded in the matrix. The nanoscale precipitates are orthogonal aligned with each other as illustrated in the upper right inset figure of Figure 8c. The inset selected SAED along [100] of Figure 8c shows only one set of diffraction spots, which indicates that the small lattice mismatch between the precipitates and the matrix cannot be resolved by SAED. Figure 8d shows an HRTEM image of the precipitates as highlighted by the red dashed box, revealing the coherent nature of the precipitates in the matrix. Besides the nanoscale precipitates in the matrix, precipitates along the grain boundary are also observed by STEM as shown in Figure S4a. The compositions of the precipitates are studied by STEM EDS mapping. The precipitates show darker contrast compared to the matrix since Mn has lower atomic number than Sn and Te. The area for STEM EDS mapping is indicated by the yellow window in Figure S4a. Figure S4b shows the element mapping for Mn, Sn,

DOI: 10.1021/jacs.5b07284
J. Am. Chem. Soc. XXXX, XXX, XXX−XXX

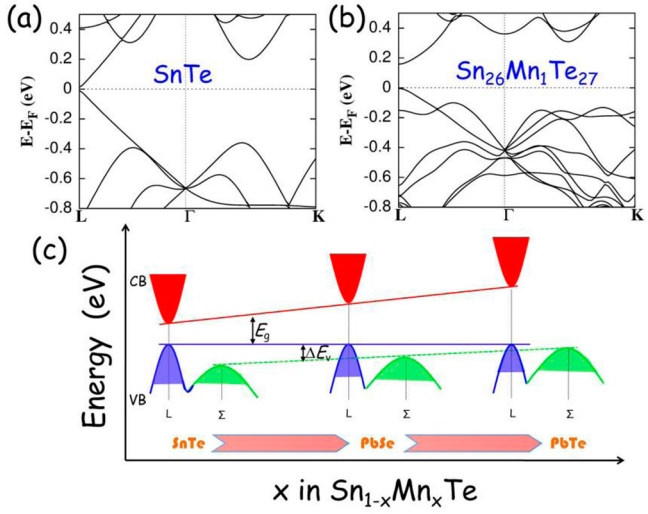

Figure 7. Calculated band structures of (a) pure SnTe and (b) ~3.7 mol% Mn-doped SnTe. A significant alteration of band structure (band gap E_g becoming larger while ΔE_v is getting smaller) can be seen as Mn is introduced into SnTe. (c) A schematic diagram of band structure evolution of SnTe as Mn content rises: when a limited Mn or Cd is introduced, the band character of SnTe becomes PbSe-like; when even higher Mn is involved (which cannot be achieved through Cd or Hg doping because of their low solubility), it becomes like PbTe.

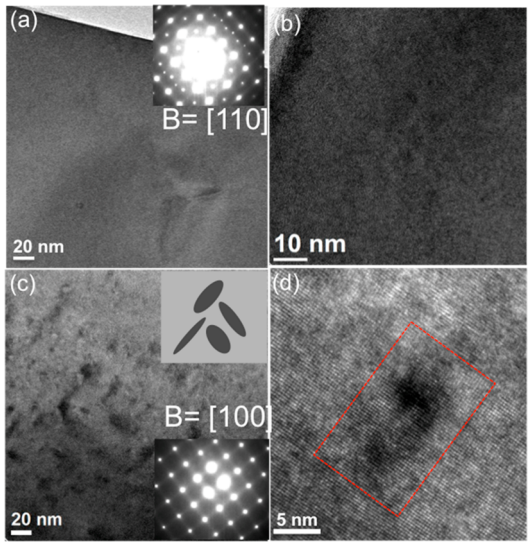

Figure 8. Electron microscopy of samples $Sn_{0.93}Mn_{0.07}Te$ and $Sn_{0.88}Mn_{0.12}Te$. (a) A medium-magnification TEM image of $Sn_{0.93}Mn_{0.07}Te$, showing no existence of precipitates. The inset is the SAED pattern with beam orientated along [110] direction. (b) HRTEM image of the area in (a), indicating good quality of the sample with minimum damage by the sample preparation. (c) Medium-magnification TEM image of sample $Sn_{0.88}Mn_{0.12}Te$ showing nanoscale precipitates orthogonal to each other, as demonstrated by the upper right inset. The lower right inset is the SAED pattern with beam oriented along the [100] orientation. (d) HRTEM image of one of the precipitates, showing coherent interfaces, highlighted by the red dashed box.

and Te. The contrast in the mappings reveals that the precipitates are rich in Mn, but deficient in Sn. Te signals in the precipitates are almost the same as in the matrix. The precipitates decrease the lattice thermal conductivity as shown in Figure 4b, which increases the figure of merit *ZT* shown in Figure 5a. The existence of the precipitates may also explain the deviation of the experimental results from the theoretical calculation based on the alloy model as shown in Figure 4d.

CONCLUDING REMARKS

MnTe solubility is relatively high in SnTe (around 9%) and it is shown to substantially decrease the energy separation between the two valence bands (L and Σ) of SnTe. This band structure modification contributes to the enhancement of Seebeck coefficient over a broad temperature range. The much higher solubility of Mn in SnTe compared to Cd and Hg makes it possible to achieve a better band convergence and produces the largest Seebeck coefficients observed for SnTe. At the same time the high Mn fraction in the lattice creates stronger point defect scattering for lower lattice thermal conductivities. The Mn-rich nanoprecipitates form when Mn exceeds its solubility limit, and results in lower than expected lattice thermal conductivities which be modeled using an alloy model. Moreover, the enlarged band gap of SnTe caused by Mn alloying greatly suppresses the bipolar conduction. These multiple beneficial effects of Mn alloying in SnTe yield a high thermoelectric figure of merit of ~1.3 at 900 K, which is among the highest reported for p-type SnTe. The high performance could make Mn-doped SnTe a robust candidate for high-temperature thermoelectric power generation when lead-free materials are desired.

ASSOCIATED CONTENT

Supporting Information

The Supporting Information is available free of charge on the ACS Publications website at DOI: 10.1021/jacs.5b07284.

Room-temperature densities (Table S1); temperature-dependent thermal diffusivities (Figure S1) and Lorenz numbers (Figure S2) for all the samples investigated in this study; thermal stability of the high-performing $Sn_{0.88}Mn_{0.12}Te$ sample as assessed by the repeatability of the thermoelectric measurements during the heating–cooling thermal cycles (Figure S3); STEM EDS mapping of precipitates at a grain boundary in sample $Sn_{0.88}Mn_{0.12}Te$ (Figure S4) (PDF)

AUTHOR INFORMATION

Corresponding Author

*m-kanatzidis@northwestern.edu

Notes

The authors declare no competing financial interest.

ACKNOWLEDGMENTS

This work was supported as part of the Revolutionary Materials for Solid State Energy Conversion, an Energy Frontier Research Center, funded by the U.S. Department of Energy, Office of Science, and Office of Basic Energy Sciences under Award Number DE-SC0001054. Transmission electron microscopy work was partially performed in the EPIC facility of the NUANCE Center at Northwestern University. Access to facilities of high-performance computational resources at the Northwestern University is acknowledged.

DOI: 10.1021/jacs.5b07284
J. Am. Chem. Soc. XXXX, XXX, XXX−XXX

REFERENCES

(1) Heremans, J. P.; Jovovic, V.; Toberer, E. S.; Saramat, A.; Kurosaki, K.; Charoenphakdee, A.; Yamanaka, S.; Snyder, G. J. *Science* **2008**, *321*, 554.

(2) (a) Biswas, K.; He, J.; Blum, I. D.; Wu, C.-I.; Hogan, T. P.; Seidman, D. N.; Dravid, V. P.; Kanatzidis, M. G. *Nature* **2012**, *489*, 414. (b) Androulakis, J.; Lin, C. H.; Kong, H. J.; Uher, C.; Wu, C. I.; Hogan, T.; Cook, B. A.; Caillat, T.; Paraskevopoulos, K. M.; Kanatzidis, M. G. *J. Am. Chem. Soc.* **2007**, *129*, 9780. (c) Bilc, D.; Mahanti, S. D.; Quarez, E.; Hsu, K. F.; Pcionek, R.; Kanatzidis, M. G. *Phys. Rev. Lett.* **2004**, *93*, 146403. (d) Bozin, E. S.; Malliakas, C. D.; Souvatzis, P.; Proffen, T.; Spaldin, N. A.; Kanatzidis, M. G.; Billinge, S. J. L. *Science* **2010**, *330*, 1660.

(3) Zhao, L. D.; Wu, H. J.; Hao, S. Q.; Wu, C. I.; Zhou, X. Y.; Biswas, K.; He, J. Q.; Hogan, T. P.; Uher, C.; Wolverton, C.; Dravid, V. P.; Kanatzidis, M. G. *Energy Environ. Sci.* **2013**, *6*, 3346.

(4) (a) Hsu, K. F.; Loo, S.; Guo, F.; Chen, W.; Dyck, J. S.; Uher, C.; Hogan, T.; Polychroniadis, E. K.; Kanatzidis, M. G. *Science* **2004**, *303*, 818. (b) Girard, S. N.; He, J. Q.; Zhou, X. Y.; Shoemaker, D.; Jaworski, C. M.; Uher, C.; Dravid, V. P.; Heremans, J. P.; Kanatzidis, M. G. *J. Am. Chem. Soc.* **2011**, *133*, 16588. (c) He, J. Q.; Girard, S. N.; Kanatzidis, M. G.; Dravid, V. P. *Adv. Funct. Mater.* **2010**, *20*, 764.

(5) Wang, H.; Bahk, J.-H.; Kang, C.; Hwang, J.; Kim, K.; Kim, J.; Burke, P.; Bowers, J. E.; Gossard, A. C.; Shakouri, A.; Kim, W. *Proc. Natl. Acad. Sci. U. S. A.* **2014**, *111*, 10949.

(6) Littlewood, P. B. *J. Phys. C: Solid State Phys.* **1980**, *13*, 4855.

(7) Rogers, L. M. *J. Phys. D: Appl. Phys.* **1968**, *1*, 845.

(8) Santhanam, S.; Chaudhuri, A. K. *Mater. Res. Bull.* **1981**, *16*, 911.

(9) Sitter, H.; Lischka, K.; Heinrich, H. *Phys. Rev. B* **1977**, *16*, 680.

(10) Schmidt, R.; Case, E.; Ni, J.; Trejo, R.; Lara-Curzio, E.; Korkosz, R.; Kanatzidis, M. *J. Mater. Sci.* **2013**, *48*, 8244.

(11) Zhang, Q.; Liao, B.; Lan, Y.; Lukas, K.; Liu, W.; Esfarjani, K.; Opeil, C.; Broido, D.; Chen, G.; Ren, Z. *Proc. Natl. Acad. Sci. U. S. A.* **2013**, *110*, 13261.

(12) Tan, G.; Zhao, L.-D.; Shi, F.; Doak, J. W.; Lo, S.-H.; Sun, H.; Wolverton, C.; Dravid, V. P.; Uher, C.; Kanatzidis, M. G. *J. Am. Chem. Soc.* **2014**, *136*, 7006.

(13) Tan, G.; Shi, F.; Hao, S.; Chi, H.; Zhao, L.-D.; Uher, C.; Wolverton, C.; Dravid, V. P.; Kanatzidis, M. G. *J. Am. Chem. Soc.* **2015**, *137*, 5100.

(14) Tan, G.; Shi, F.; Doak, J. W.; Sun, H.; Zhao, L.-D.; Wang, P.; Uher, C.; Wolverton, C.; Dravid, V. P.; Kanatzidis, M. G. *Energy Environ. Sci.* **2015**, *8*, 267.

(15) Tan, G.; Shi, F.; Sun, H.; Zhao, L.-D.; Uher, C.; Dravid, V. P.; Kanatzidis, M. G. *J. Mater. Chem. A* **2014**, *2*, 20849.

(16) Zhou, M.; Gibbs, Z. M.; Wang, H.; Han, Y.; Xin, C.; Li, L.; Snyder, G. J. *Phys. Chem. Chem. Phys.* **2014**, *16*, 20741.

(17) Chen, Y.; Nielsen, M. D.; Gao, Y.-B.; Zhu, T.-J.; Zhao, X.; Heremans, J. P. *Adv. Energy Mater.* **2012**, *2*, 58.

(18) Banik, A.; Biswas, K. *J. Mater. Chem. A* **2014**, *2*, 9620.

(19) Banik, A.; Shenoy, U. S.; Anand, S.; Waghmare, U. V.; Biswas, K. *Chem. Mater.* **2015**, *27*, 581.

(20) Xu, E. Z.; Li, Z.; Martinez, J. A.; Sinitsyn, N.; Htoon, H.; Li, N.; Swartzentruber, B.; Hollingsworth, J. A.; Wang, J.; Zhang, S. X. *Nanoscale* **2015**, *7*, 2869.

(21) Han, M.-K.; Androulakis, J.; Kim, S.-J.; Kanatzidis, M. G. *Adv. Energy Mater.* **2012**, *2*, 157.

(22) Han, M.-K.; Zhou, X.; Uher, C.; Kim, S.-J.; Kanatzidis, M. G. *Adv. Energy Mater.* **2012**, *2*, 1218.

(23) Brebrick, R. F.; Strauss, A. J. *Phys. Rev.* **1963**, *131*, 104.

(24) Kafalas, J. A.; Brebrick, R. F.; Strauss, A. J. *Appl. Phys. Lett.* **1964**, *4*, 93.

(25) Brebrick, R. F. *J. Phys. Chem. Solids* **1963**, *24*, 27.

(26) Singh, D. J. *Funct. Mater. Lett.* **2010**, *03*, 223.

(27) Vedeneev, V. P.; Krivoruchko, S. P.; Sabo, E. P. *Semiconductors* **1998**, *32*, 241.

(28) Martinez, G.; Schlüter, M.; Cohen, M. L. *Phys. Rev. B* **1975**, *11*, 651.

(29) Pei, Y.-L.; Liu, Y. *J. Alloys Compd.* **2012**, *514*, 40.

(30) Pei, Y.; Wang, H.; Gibbs, Z. M.; LaLonde, A. D.; Snyder, G. J. *NPG Asia Mater.* **2012**, *4*, e28.

(31) Łusakowski, A.; Bogusławski, P.; Radzyński, T. *Phys. Rev. B: Condens. Matter Mater. Phys.* **2011**, *83*, 115206.

(32) Neuwirth, J.; Jantsch, W.; Palmetshofer, L.; Zulehner, W. *J. Phys. C: Solid State Phys.* **1986**, *19*, 2475.

(33) Eggenkamp, P. J. T.; Vennix, C. W. H. M.; Story, T.; Swagten, H. J. M.; Swüste, C. H. W.; de Jonge, W. J. M. *J. Appl. Phys.* **1994**, *75*, 5728.

(34) Vennix, C. W. H. M.; Frikkee, E.; Swagten, H. J. M.; Kopinga, K.; de Jonge, W. J. M. *J. Appl. Phys.* **1991**, *69*, 6025.

(35) Łazarczyk, P.; Story, T.; Jędrzejczak, A.; Gałązka, R. R.; Mac, W.; Herbich, M.; Stachow-Wójcik, A. *J. Magn. Magn. Mater.* **1997**, *176*, 233.

(36) Gad, S. A.; Moustafa, A. M.; Boshta, M.; Abo El-Soud, A. M.; Farag, B. S. *Phys. B* **2010**, *405*, 1495.

(37) Freik, D.; Galushchak, M.; Ivanishin, I.; Shperun, V.; Zapukhlyak, R.; Pyts, M. *Semicond. Phys. Quantum Electron. Optoelectron.* **2000**, *3*, 287.

(38) Zhao, L.-D.; Dravid, V. P.; Kanatzidis, M. G. *Energy Environ. Sci.* **2014**, *7*, 251.

(39) Wang, H.; Gibbs, Z. M.; Takagiwa, Y.; Snyder, G. J. *Energy Environ. Sci.* **2014**, *7*, 804.

(40) Pei, Y.; LaLonde, A.; Iwanaga, S.; Snyder, G. J. *Energy Environ. Sci.* **2011**, *4*, 2085.

(41) Borup, K. A.; de Boor, J.; Wang, H.; Drymiotis, F.; Gascoin, F.; Shi, X.; Chen, L.; Fedorov, M. I.; Muller, E.; Iversen, B. B.; Snyder, G. J. *Energy Environ. Sci.* **2015**, *8*, 423.

(42) Tan, G.; Wang, S.; Yan, Y.; Li, H.; Tang, X. *J. Alloys Compd.* **2012**, *513*, 328.

(43) Tan, G.; Liu, W.; Chi, H.; Su, X.; Wang, S.; Yan, Y.; Tang, X.; Wong-Ng, W.; Uher, C. *Acta Mater.* **2013**, *61*, 7693.

(44) Nolas, G.; Sharp, J.; Goldsmid, H. *Thermoelectrics: Basic Principles and New Materials Developments*; Springer Science & Business Media: New York, 2001.

(45) Tan, G.; Wang, S.; Tang, X.; Li, H.; Uher, C. *J. Solid State Chem.* **2012**, *196*, 203.

(46) Perdew, J. P.; Burke, K.; Ernzerhof, M. *Phys. Rev. Lett.* **1996**, *77*, 3865.

(47) Kresse, G.; Furthmüller, J. *Phys. Rev. B: Condens. Matter Mater. Phys.* **1996**, *54*, 11169.

(48) Inoue, M.; Yagi, H.; Muratani, T.; Tatsukawa, T. *J. Phys. Soc. Jpn.* **1976**, *40*, 458.

(49) Dash, K.; Tripathi, G. S. *Semicond. Sci. Technol.* **2009**, *24*, 115004.

(50) Popescu, V.; Zunger, A. *Phys. Rev. Lett.* **2010**, *104*, 236403.

(51) Popescu, V.; Zunger, A. *Phys. Rev. B: Condens. Matter Mater. Phys.* **2012**, *85*, 085201.

(52) Girard, S. N.; He, J.; Zhou, X.; Shoemaker, D.; Jaworski, C. M.; Uher, C.; Dravid, V. P.; Heremans, J. P.; Kanatzidis, M. G. *J. Am. Chem. Soc.* **2011**, *133*, 16588.

(53) Androulakis, J.; Hsu, K. F.; Pcionek, R.; Kong, H.; Uher, C.; D'Angelo, J. J.; Downey, A.; Hogan, T.; Kanatzidis, M. G. *Adv. Mater.* **2006**, *18*, 1170.

(54) Arachchige, I. U.; Wu, J.; Dravid, V. P.; Kanatzidis, M. G. *Adv. Mater.* **2008**, *20*, 3638.

(55) Dudkin, L. D.; Gaidukova, W. S.; Ostrovskaya, L. M. *Inorg. Mater.* **1971**, *7*, 1332.

(56) Hemstreet, L. A. *Phys. Rev. B* **1975**, *12*, 1212.

(57) Rogacheva, E. I. *J. Phys. Chem. Solids* **2008**, *69*, 259.

(58) Goldsmid, H. J. *Applications of Thermoelectricity*; Butler & Tanner Ltd.: London, 1960.

(59) Klemens, P. G. *Phys. Rev.* **1960**, *119*, 507.

(60) Bukshpan, S. *Solid State Commun.* **1968**, *6*, 477.

(61) Bauer Pereira, P.; Sergueev, I.; Gorsse, S.; Dadda, J.; Müller, E.; Hermann, R. P. *Phys. Status Solidi B* **2013**, *250*, 1300.

(62) Abeles, B. *Phys. Rev.* **1963**, *131*, 1906.

(63) Eshelby, J. D. *Acta Metall.* **1955**, *3*, 487.

DOI: 10.1021/jacs.5b07284
J. Am. Chem. Soc. XXXX, XXX, XXX−XXX

(64) Anderson, D. L.; Anderson, O. L. *J. Geophys. Res.* **1970**, *75*, 3494.
(65) Anderson, O. L.; Nafe, J. E. *J. Geophys. Res.* **1965**, *70*, 3951.
(66) Toher, C.; Plata, J. J.; Levy, O.; de Jong, M.; Asta, M.; Nardelli, M. B.; Curtarolo, S. *Phys. Rev. B: Condens. Matter Mater. Phys.* **2014**, *90*, 174107.
(67) Yan, X.; Joshi, G.; Liu, W.; Lan, Y.; Wang, H.; Lee, S.; Simonson, J. W.; Poon, S. J.; Tritt, T. M.; Chen, G.; Ren, Z. F. *Nano Lett.* **2011**, *11*, 556.
(68) Liu, W.; Yin, K.; Su, X.; Li, H.; Yan, Y.; Tang, X.; Uher, C. *Intermetallics* **2013**, *32*, 352.
(69) Joshi, G.; Lee, H.; Lan, Y.; Wang, X.; Zhu, G.; Wang, D.; Gould, R. W.; Cuff, D. C.; Tang, M. Y.; Dresselhaus, M. S.; Chen, G.; Ren, Z. *Nano Lett.* **2008**, *8*, 4670.
(70) Tan, G.; Zheng, Y.; Tang, X. *Appl. Phys. Lett.* **2013**, *103*, 183904.
(71) Lu, X.; Morelli, D. T.; Xia, Y.; Zhou, F.; Ozolins, V.; Chi, H.; Zhou, X.; Uher, C. *Adv. Energy Mater.* **2013**, *3*, 342.
(72) Galushchak, M.; Freik, D.; Ivanyshyn, I.; Lisak, A.; Pyts, M. *J. Thermoelectr.* **2000**, *1*, 42.
(73) Pei, Y.; Shi, X.; LaLonde, A.; Wang, H.; Chen, L.; Snyder, G. J. *Nature* **2011**, *473*, 66.
(74) Veis, A.; Kaidanov, V.; Kuteinikov, R.; Nemov, S.; Rudenko, S.; Ukhanov, Y. I. *Sov. Phys. Semiconductors* **1978**, *12*, 161.
(75) Allgaier, R. S.; Houston, B. B. *J. Appl. Phys.* **1966**, *37*, 302.
(76) Putley, E. H. *J. Phys. C: Solid State Phys.* **1975**, *8*, 1837.
(77) Pei, Y.; Wang, H.; Snyder, G. J. *Adv. Mater.* **2012**, *24*, 6125.
(78) Wang, H.; Pei, Y.; LaLonde, A. D.; Snyder, G. J. *Adv. Mater.* **2011**, *23*, 1366.
(79) Zhao, L.-D.; He, J.; Wu, C.-I.; Hogan, T. P.; Zhou, X.; Uher, C.; Dravid, V. P.; Kanatzidis, M. G. *J. Am. Chem. Soc.* **2012**, *134*, 7902.
(80) Thompson, R. K. C.; Edington, J. W. *Electron Diffraction in Electron Microscope*; Technical Library: Eindhoven, 1977.

DOI: 10.1021/jacs.5b07284
J. Am. Chem. Soc. XXXX, XXX, XXX−XXX